Space Weather

RESEARCH ARTICLE
10.1029/2018SW001865

Special Section:
Space Weather Events of 4-10 September 2017

Formation and Evolution of Low-Latitude *F* Region Field-Aligned Irregularities During the 7–8 September 2017 Storm: Hainan Coherent Scatter Phased Array Radar and Digisonde Observations

Han Jin[1,2], Shasha Zou[2], Gang Chen[1], Chunxiao Yan[1,3], Shaodong Zhang[1], and Guotao Yang[3]

[1]Electronic Information School, Wuhan University, Wuhan, China, [2]Department of Climate and Space Sciences and Engineering, University of Michigan, Ann Arbor, MI, USA, [3]National Space Science Center, Chinese Academy of Sciences, Beijing, China

Key Points:
- Low-latitude ionospheric observations by seven-beam (east-west plane) VHF radar operated at Fuke, China, and a nearby digisonde
- Storm-induced PPEF is responsible for postsunset FAIs, and substorm-related overshielding *E* field leads to postmidnight FAIs
- Plasma bubble irregularities showed dominantly westward drift rather than the eastward drift normally observed under quiet conditions

Correspondence to:
H. Jin,
jinhan@whu.edu.cn

Citation:
Jin, H., Zou, S., Chen, G., Yan, C., Zhang, S., & Yang, G. (2018). Formation and evolution of low-latitude *F* region field-aligned irregularities during the 7–8 September 2017 storm: Hainan coherent scatter phased array radar and digisonde observations. *Space Weather*, *16*, 648–659. https://doi.org/10.1029/2018SW001865

Received 13 MAR 2018
Accepted 16 MAY 2018
Accepted article online 21 MAY 2018
Published online 15 JUN 2018

Abstract In this paper, we present a study of the low-latitude field-aligned irregularities formation and evolution during the 7–8 September 2017 geomagnetic storm by analyzing data of the very high frequency coherent radar installed at Fuke, Hainan Island of China (19.5°N, 109.1°E; magnetic latitude 9.58°N) and a colocated Digisonde Portable Sounder. The prompt penetration of eastward interplanetary electric field associated with sudden southward turning of the interplanetary magnetic field Bz resulted in large ascent of the *F* layer, making conducive conditions at the bottomside of the layer for the growth of Rayleigh-Taylor instability and the development of the plasma irregularities in the postsunset hours. The irregularities persisted into the postmidnight sector when the southward interplanetary magnetic field Bz gradually decreased to the quiet time values. In addition, the base height of *F* layer at Fuke also showed a large elevation after midnight during two consecutive substorm onsets, suggesting that the substorm-induced overshielding penetration electric field may take over and modify the ambient zonal electric field in low-latitude ionosphere and induce the irregularities in the postmidnight sector. Moreover, different from the quiet time eastward movement of the irregularities observed over Fuke, the storm time irregularities displayed no zonal drift at the initial period and subsequently began drifting westward. The reversal of background plasma zonal drift velocity observed by Hainan digisonde characterized the storm time zonal drift pattern of the irregularities.

1. Introduction

The equatorial/low-latitude *F* region field-aligned irregularities (FAIs), also known as equatorial/low-latitude spread *F*, have been extensively studied for decades by using various instruments, such as VHF radars (e.g., Li et al., 2013; Tsunoda, 1980; Woodman & LaHoz, 1976; Yokoyama & Fukao, 2006), ionosondes (Abdu et al., 2003; W. S. Chen et al., 2006; Lee et al., 2005), optical airglow imager (Hickey et al., 2015; Otsuka et al., 2004; Sobral et al., 2009), Global Positioning System scintillation measurements (Li et al., 2010; Pi et al., 1997), and in situ satellites (Basu et al., 2001; Burke et al., 2004; Huang et al., 2012). Plasma irregularities in the ionosphere may cause rapid variations in phase and amplitude of radio signals and lead to detrimental effect on navigation and communication system (Woodman, 2009, and references therein). Therefore, it is important to understand the underlying generation mechanism of these ionospheric irregular structures.

The seasonal, longitudinal, and solar cycle dependence of the equatorial/low-latitude FAIs occurrences have been intensively investigated (e.g., Burke et al., 2004; Huang et al., 2014; Kil & Heelis, 1998; Rastogi, 1980), but the day-to-day and storm time variability of the FAIs occurrences is still a challenging problem for the forecast of equatorial/low-latitude spread *F*. It has been generally accepted that ionospheric irregularities are mainly generated via the generalized Rayleigh-Taylor (R-T) instability (Ott, 1978) that may develop at the bottomside of the *F* layer and rapidly arise to the topside ionosphere. The equatorial/low-latitude FAIs usually occur during postsunset hours due to the evening prereversal enhancement (PRE) of zonal (eastward) electric field/vertical plasma drift (Woodman, 1970), which provides favorable conditions for the growth of the R-T instability by lifting the lower *F* layer to higher altitudes where the ion-neutral collision frequency is lower.

The PRE of zonal electric field/vertical plasma drift is one of the most important factors for facilitating quiet time FAIs generation, but during storm time, other factors can also lead to perturbation in zonal electric field and thus facilitate the generation of FAIs.

The generation or suppression of equatorial/low-latitude FAIs during geomagnetic disturbances, in particular, geomagnetic storms, are very complicated and have been studied extensively (Abdu, 2012; Martinis et al., 2005, and references therein). Under geomagnetic disturbance conditions, the equatorial/low-latitude zonal electric field, which controls the occurrence of FAIs, might be modified by two important drivers, that is, prompt penetration of electric field (PPEF) from high-latitude to low-latitude/equatorial regions (Nishida, 1968) and disturbance dynamo electric field (DDEF) driven by disturbed global thermospheric circulation due to Joule heating (Blanc & Richmond, 1980).

The equatorward penetration of dawn-dusk electric field (PPEF) occurs almost simultaneously with the sudden southward excursion of the interplanetary magnetic field (IMF) Bz and produce short-term (tens of minutes to 1–2 hr) perturbations in the equatorial/low-latitude zonal electric field. The PPEF is eastward (westward) on the dayside (nightside), which has the same polarity with the quiet time ambient zonal electric field at equatorial/low-latitude ionosphere. The eastward PPEF superposed on the normal PRE of zonal electric field in evening hours will enhance the vertical plasma drift in *F* region, consequently inducing the equatorial/low-latitude FAIs generation. Shielding electric field gradually builds up in the inner magnetosphere region after the enhanced convection, and the PPEF will be gradually shielded (Kikuchi et al., 2008). However, the IMF Bz usually fluctuates and, therefore, the equatorial electric field is rarely balanced. If there is a sudden IMF Bz northward turning or a substorm onset, the PPEF will reduce and the shielding electric field may dominate, then the total electric field may now become dusk-to-dawn, that is, westward (eastward) on the dayside (nightside), which is opposite of the dawn-dusk PPEF (Fujita et al., 2010; Hashimoto et al., 2011; Kikuchi et al., 2003; Wei et al., 2009). On the other hand, the DDEF occurs with a few hours of delay from the beginning of the storm and usually lasts for longer period than the PPEF. In general, the DDEF has westward polarity in the evening hours and can diminish or even reverse the normal PRE of zonal electric field in equatorial/low-latitude ionosphere, which then inhibit the development of the FAIs. Therefore, the excitation or inhibition of equatorial/low-latitude FAIs during the geomagnetic storm depends on the interplay between PPEF and DDEF. For instance, generation of FAIs during the main phase of the geomagnetic storm due to eastward PPEF in the dusk sector have been reported (i.e., Abdu et al., 2003, Basu et al., 2001, Patra et al., 2016, Tulasi Ram et al., 2008). Abdu et al. (1997) reported the inhibition of the equatorial PRE and the postsunset spread *F* due to the westward DDEF in the evening during the storm recovery. Recently, Rajesh et al. (2017) discussed the inhibition of the irregularities over Taiwan during the 2015 St. Patrick's Day storm, and they suggested that the westward overshielding electric field resulting from transient northward turning of IMF Bz around the dusk was responsible for the FAIs inhibition.

The suppression or initiation of the equatorial/low-latitude FAIs during the geomagnetic storm largely hinges on the competitive effects of these perturbation electric fields mentioned above. In this paper, we investigate the development of the low-latitude ionospheric zonal electric field and irregularities during the 7–8 September 2017 storm. Our observations are primarily based on the VHF coherent radar and the digisonde installed at Fuke, Hainan Island of China (19.5°N, 109.1°E; magnetic latitude 9.58°N). A brief description of the instruments is presented in section 2. In section 3, we briefly introduce the characteristics of the 7–8 September 2017 geomagnetic storm and then present the low-latitude ionospheric irregularities as well as the background plasma condition during the storm. Sections 4 and 5 give the discussion and conclusion, respectively. The results we present here contribute to improving current understanding of the storm time low-latitude plasma irregularities generation and evolution.

2. Instruments

Figure 1 shows the location and field of view (FoV) of the Hainan coherent scatter phased array radar (HCOPAR) located at Fuke, Hainan Island of China (19.5°N, 109.1°E; magnetic latitude 9.58°N). It is one of the most important radio systems of Chinese Meridian Project (Wang, 2010). It operates at 47 MHz with 54-kW peak power and 2-MHz bandwidth to detect the 3.2-m-scale field-aligned irregularities in the low-latitude ionosphere (G. Chen et al., 2017). Its antenna array consisted of 18 ×4 five-element linear-polarized Yagi antennas covering an area of 2,000 m^2. As shown in Figure 1, the HCOPAR has an active phased array

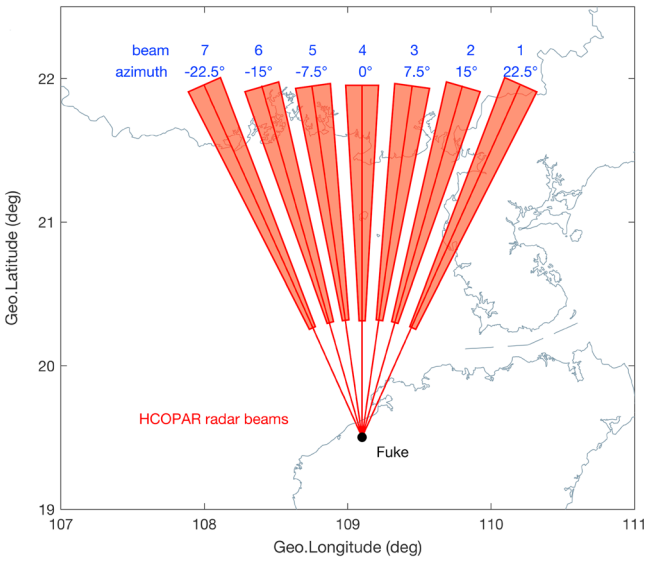

Figure 1. Map projection of the seven beam directions of Hainan coherent scatter phased array radar (HCOPAR). Each beam is separated by 7.5° in azimuth and Beam 4 points to due geographic north.

system, which allows the radar beam to steer in seven directions, each separated by 7.5° in azimuth ranging from 22.5° (Beam 1) to −22.5° (Beam 7) around the geographic north. The central beam (Beam 4) of the radar points to the geographic north, which deviates from geomagnetic north only by 1°. The azimuth and elevation angles of the seven beams are (−22.5°,59.72°), (−15°,60.70°), (−7.5°,61.24°), (0°,61.36°), (7.5°,61.06°), (15°,60.35°), and (22.5°,59.15°). The central direction of the seven radar beams is almost perpendicular to the local geomagnetic field at altitudes of the ionospheric *E* and *F* regions to ensure the simultaneous observations of *E* and *F* region field-aligned irregularities. The range resolution of the radar measurement is 0.711 km. The arrangement of the seven radar beams provides a view of two-dimensional structures of the backscatter echoes. The time duration to complete one azimuth scan from Beam 1 to Beam 7 is approximately 120 s. The fan sector maps can be constructed every 2 min by combining the signal-to-noise ratio (SNR) from seven beams, revealing the spatial and temporal evolutions of the ionospheric irregularities.

The background ionospheric condition and drifts are recorded by a colocated Digisonde Portable Sounder (DPS-4D; Reinisch et al., 2009) at Hainan. The Hainan digisonde routinely operates every 15 min to obtain an ionogram, and it was operated every 5 min to obtain an ionogram during the storm days. The virtual height of the bottomside *F* layer, *h*′*F*, can be manually scaled from an ionogram. The mean vertical and zonal drift velocities in the *F* region can be calculated from Doppler skymap according to the angle of arrival and Doppler velocity of the echoes (Reinisch et al., 1998).

3. Observations

3.1. Characteristics of the 7–8 September 2017 Storm with Double Main Phase

Figures 2a–2f present the 1-min resolution data of solar wind velocity, density, dynamic pressure, IMF Bz, interplanetary electric field (IEF) Ey, and the symmetric index (SYM/H), respectively, during 7–8 September 2017. The data are obtained from the OMNI Web site, and they have been corrected for the propagation delay up to the Earth's bow shock. This geomagnetic storm was caused by multiple interplanetary coronal mass ejections, including a shocked-interplanetary coronal mass ejection (Shen et al., 2017, 2018). The IEF Ey component is calculated as Ey = −*V*sw ×Bz, where *V*sw is the sunward solar wind velocity component. Sharp enhancements in the solar wind velocity, density and dynamic pressure were observed at around 23:11 UT on 7 September 2017, indicating the arrival of an interplanetary shock. The main phase of the storm commenced at ~23:31 UT on 7 September 2017 with a steep southward excursion of the IMF Bz component to −31.2 nT and the IEF Ey component reached ~21 mV/m. The first intensification of the geomagnetic storm with the minimum SYM/H of −146 nT occurred at ~01:10 UT on 8 September 2017. The IMF Bz remained southward for more than 2 hr, became northward at ~02:30 UT on 8 September and remained northward for ~9 hr except for five transient southward turnings. Another large and rapid IMF Bz southward turning occurred at 11:55 UT, reaching ~ − 17.4 nT and the IEF Ey component became eastward rapidly to the peak value of 13.76 mV/m. This second large southward turning of IMF Bz leads to the second main phase of the storm and another dip with SYM/H index reaching ~ − 115 nT. We focus on observations obtained during the second main phase when it was nighttime over our observing locations.

3.2. Ionospheric Irregularities and Background Condition During the Storm

Figure 3 shows the virtual height (*h*′*F*) variations of bottomside *F* layer, vertical drift velocity, and east (positive)-west (negative) drift velocity in the ionospheric *F* region obtained from the Hainan digisonde during 10:00–19:00 UT on 7 (blue) and 8 (red) September 2017. Because the storm initiated later than 19 UT on 7 September 2017, the period up to this time can be considered as quiet time for comparison with storm time conditions. It is clear that the bottomside *F* layer went up significantly, that is, by 150 km (marked with arrow a), after ~11:40 UT on 8 September, that is, right after the second IMF Bz southward turning, and

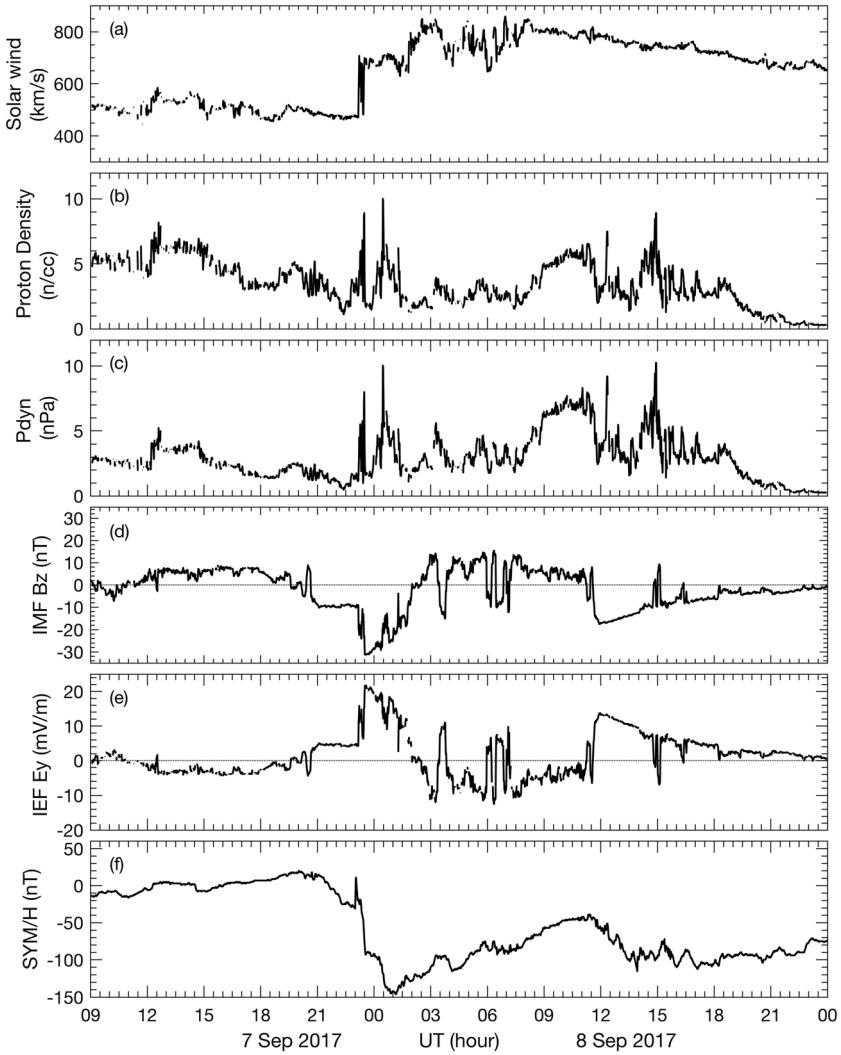

Figure 2. Temporal variations of (a) solar wind velocity (km/s), (b) solar wind density (n/cm^3), (c) solar wind dynamic pressure (nPa), (d) *Z* component of interplanetary magnetic field, interplanetary magnetic field (IMF) Bz (nT), (e) interplanetary electric field (IEF) Ey component, IEF Ey (mV/m), and (f) the symmetric index, SYM/H index (nT) during 7–8 September 2017.

reached a peak height of 387 km at ~12:35 UT in Figure 3a. Two more obvious ascending motions were observed during 13:50–14:20 UT and 17:00–17:45 UT (marked with arrows b and c, respectively). It is worth mentioning that the third uplifting of the bottomside *F* layer occurred after local midnight, which will be discussed in more detail in the next section in terms of the cause of perturbation electric field in postmidnight sector. During the three episodes of the *F* layer uplift due to positive vertical flow, shown in Figure 3b, the peak vertical drift velocity reached values of 145.8 m/s, 169.7 m/s, and 121.8 m/s, respectively. As shown in Figure 3c, the zonal drift velocity was steadily negative, that is, westward varying from about −16 to −200 m/s on 8 September after ~12:45 UT, before which the zonal drift of the background plasma fluctuated between eastward and westward. In contrast, the nighttime zonal drift of the background plasma on 7 September was mostly eastward.

The altitude-time variations of SNR and line-of-sight Doppler velocity of the FAIs observed on 8 September 2017 by Beam 4 of the HCOPAR are presented in Figures 4a and 4b, respectively. As shown in Figure 4a, seven groups of FAIs echoes were observed and are labeled from A to G. A small echo (labeled with A) started to emerge at ~12:37 UT (LT = UT + 7.3 hr) at altitudes from 330 to 370 km. Then an upwelling plume-like structure of the FAIs echoes (labeled with B) appeared at ~13:15 UT with durations of about 80 min, covering the altitudes from 305 to 460 km. At ~13:47 UT, another upwelling plume-like structure of the FAIs echoes

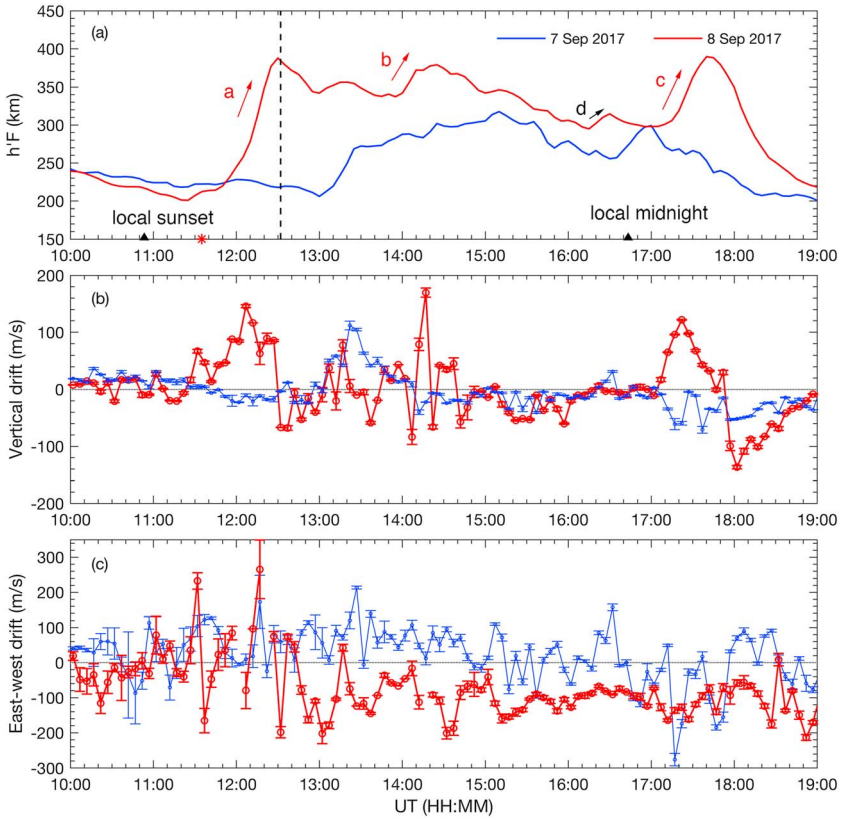

Figure 3. Time variations of (a) virtual height of bottomside *F* layer, *h'F* (km), (b) vertical drift velocity of the *F* layer (m/s), and (c) east-west drift velocity of the *F* layer (m/s) observed by Hainan digisonde on 7 (blue) and 8 (red) September 2017 during 10:00–19:00 UT. The red asterisk indicates the time when interplanetary electric field Ey suddenly turned eastward. The vertical dashed line indicates the initial time of the field-aligned irregularities observed by the Hainan coherent scatter phased array radar. Local sunset and midnight are marked with two black triangles. Error bars represent the velocity spread.

(labeled with C) was observed at higher altitudes from 510 to 590 km and the echo intensity was much weaker than Group B. Plumes in Group D started at ~14:57 UT at altitudes from 360 to 560 km with durations of about 15 min. Group E of the FAIs echoes followed closely with stronger intensity and lower-altitude ranges than Group D. Around midnight, Group F of the FAIs echoes appeared at around 400 km and showed descending pattern over time. During postmidnight hours, the HCOPAR still recorded a strip-like structure of FAIs echoes (labeled with G). Group G of the FAIs echoes initiated at ~17:15 UT at altitude of ~540 km and displayed similar descending pattern as Group F. Because Beam 4 of the HCOPAR is basically measuring within a magnetic meridional plane, the line-of-sight Doppler velocity measured along Beam 4 purely represents meridional (northward and upward or southward and downward) movement, rather than a combination of zonal and meridional velocity components of FAIs drift. As displayed in Figure 4b, the line-of-sight Doppler velocities of the postsunset FAIs echoes were mainly positive (varying from ~20 to ~100 m/s) except for the narrow descending structures in Group B, indicating that the majority of the FAIs was moving away (northward and upward) from the radar. The large upward velocities of the upwelling plume structures suggested that these FAIs were still in growth phase. The Doppler velocity of postmidnight Group G was mostly negative (−20 to −2 m/s), suggesting the irregularity was moving toward (southward and downward) the radar.

In order to investigate the spatial distribution and the zonal drift direction of the FAIs, the altitude-time-SNR plots of the FAIs echoes observed in different beam directions (from Beam 1 to Beam 7) are displayed from top to bottom in Figures 5a–5g. Considering the different formation location (i.e., inside or outside of the radar beams) of the FAIs echoes, they can be divided into two types, Type 1 (Groups A, B, and E in Figure 4a) and Type 2 (Groups C, D, F, and G in Figure 4a). Type 1 echoes were freshly generated within the FoV of the

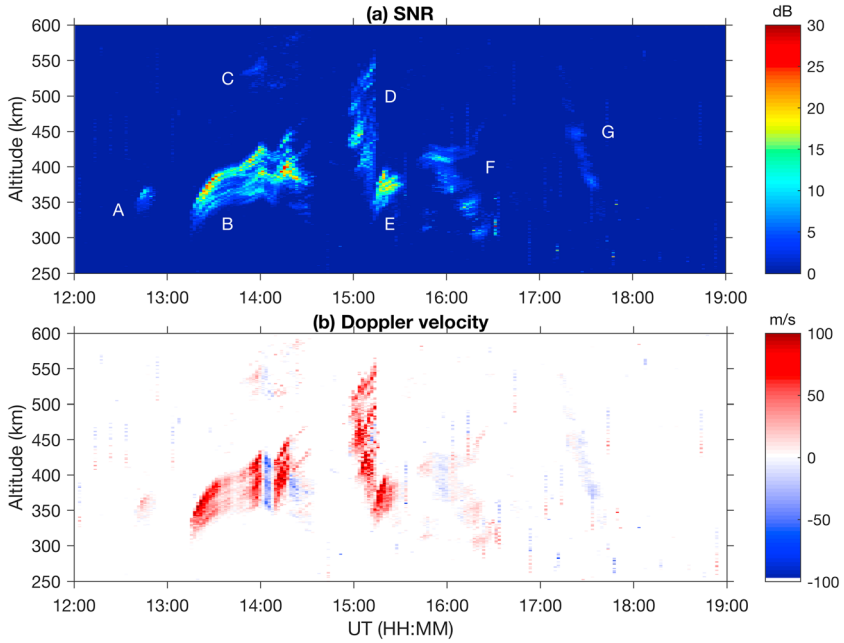

Figure 4. Altitude-time variations of (a) signal-to-noise ratio (SNR; dB) and (b) line-of-sight Doppler velocity (m/s) of the field-aligned irregularities (FAIs) observed on 8 September 2017 in Beam 4 of the Hainan coherent scatter phased array radar. Seven groups of FAIs are labeled with A–G. Positive (negative) velocity represents the FAIs moving away (toward) the radar.

HCOPAR and were still in their growth phase. Type 2 echoes were generated elsewhere and then drifting into the FoV of the HCOPAR. Type 2 FAIs echoes in this case were mostly in decaying phase, because the echo intensity became weaker when moving across the radar beams. The zonal movement of the FAIs in Beams 5–7 during 12:45–13:20 UT was not clear, but the other FAIs echoes exhibited obvious westward drift, appearing first in the easternmost beams and later in western beams. This westward moving feature is different from the typical postsunset eastward movement observed by HCOPAR over the past few years (see, e.g., Figure 11 in G. Chen et al., 2017). This is consistent with the westward drifting of the background plasma after ~12:45 UT observed in Figure 3c. The zonally motionless FAIs echoes occurred during the period of eastward wind or nearly zero zonal wind.

To illustrate the spatial distribution of the irregularities, we projected the FAIs echo intensity from different beams onto the zonal-vertical plane to generate the fan sector maps by using two-dimension interpolation method. The time sequence of two-dimensional fan sector maps of FAIs echo SNR from 13:09 UT to 14:45 UT on 8 September displayed in Figure 6 provides us a good view of the freshly generated type of the FAIs, that is, Type 1 (Group B in Figure 4a). An echo appeared in the central FoV of HCOPAR at 13:21 UT at the altitudes from 320 to 356 km, and then it expanded to higher altitudes with increasing echo intensity. Meanwhile, the fan sector maps show a clear westward movement of the FAIs echoes. These maps have been used to help the classification of the FAIs types.

4. Discussion

4.1. Postsunset FAIs

In previous section, we have presented our observations of the FAIs in the low-latitude ionospheric *F* region recorded by HCOPAR during the second main phase of the geomagnetic storm on 7–8 September 2017. As shown in Figure 2, the IEF Ey turned eastward due to the second large sudden southward turning of IMF Bz at 11:35 UT on 8 September 2017. Right after that, the base height of the *F* layer at Fuke started ascending rapidly and reached to a peak altitude of ~387 km, which was remarkably higher compared to its typical quiet day enhancement during postsunset hours on 7 September. Subsequently, the *F* region FAIs started to emerge just a few minutes later than the time of peak uplift of *h*′*F* at Fuke as indicated in Figure 3a. The

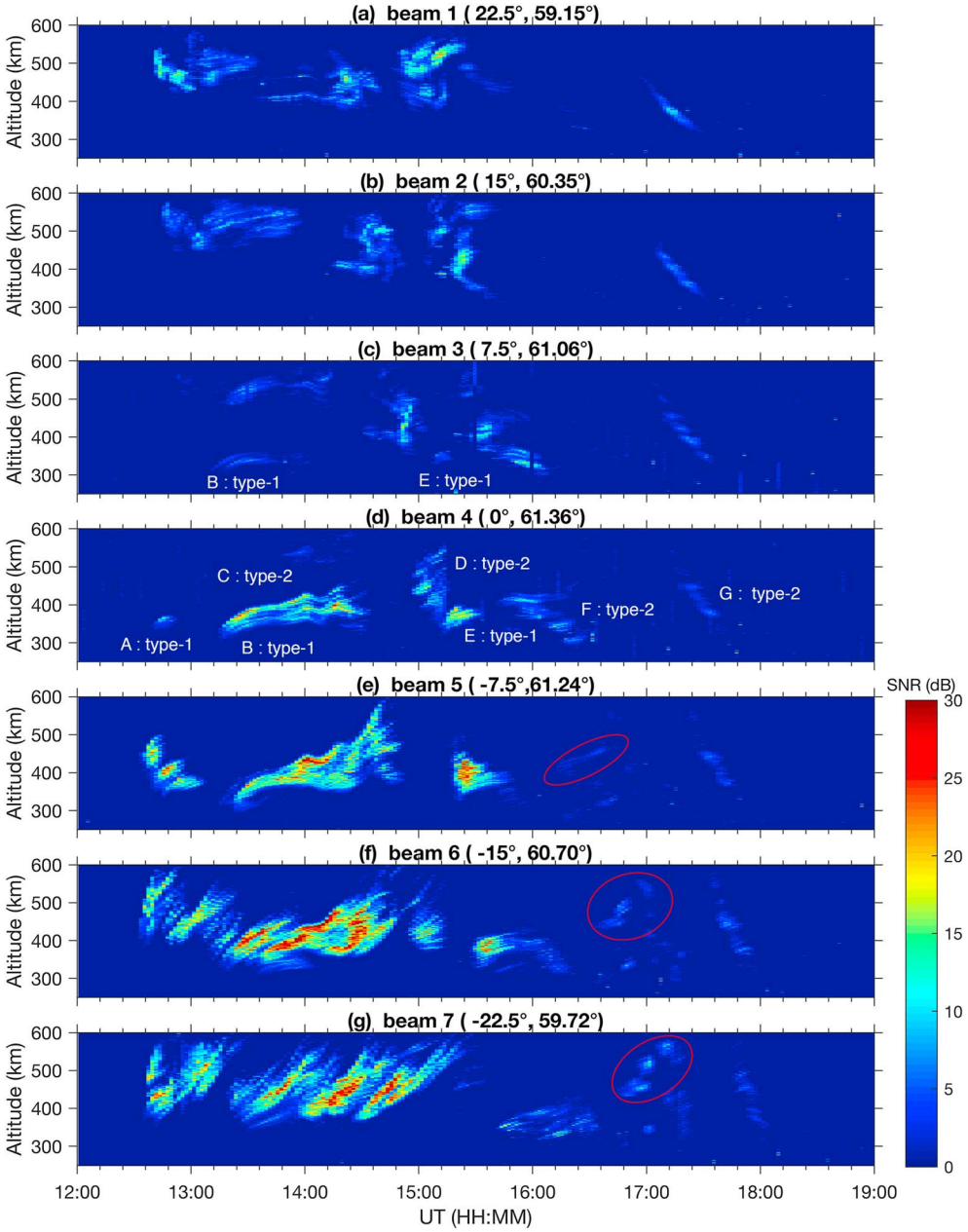

Figure 5. (a-g) Altitude-time-signal-to-noise ratio (SNR) plot of the field-aligned irregularities echoes from different beam directions (between Beam 1 and Beam 7 at interval angle of 7.5°) from top to bottom. The Groups A, B, and E were freshly generated within the field of view of the radar and they are labeled as Type 1 echoes. The Groups C, D, F, and G in Beam 4 were first recorded by the easternmost beam, that is, Beam 1, and they moved westward with decreasing echo intensity. These echoes are Type 2 field-aligned irregularities, which were generated further east of Beam 1 and then drifted into the field of view of the radar. Each subdivision within one hour represents 12 min spacing.

substantial upward movement of bottomside *F* layer generated favorable conditions for the growth of the R-T instability, which is believed to play an important role in inducing low-latitude plasma irregularities (Heelis, 2004, and references therein). This sudden uplift of bottomside *F* layer provides evidence for an enhancement of eastward electric field at Fuke and the timing of the eastward electric field enhancement agrees very well with the IEF increase based on the solar wind and IMF measurements. Therefore, we conclude that the strong eastward IEF penetrated to low-latitude ionosphere, uplifted the bottomside *F* layer to higher altitudes and triggered the postsunset FAIs. Aa et al. (2018) studied the widely extended

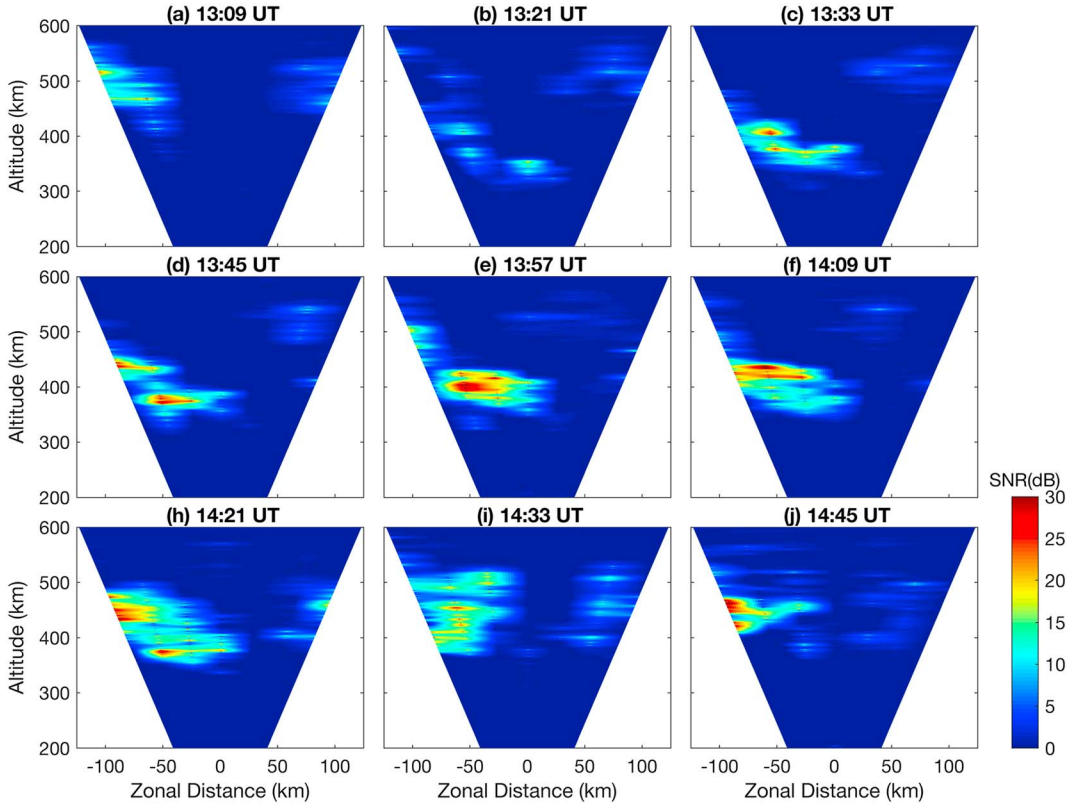

Figure 6. (a–j) Fan sector maps of the backscattered echo signal-to-noise ratio in the zonal-vertical plane between 13:09 and 14:45 UT with a time step of 12 min on 8 September 2017 showing the freshly generated type of the field-aligned irregularities (Group B in Figure 4a). The initiation can be seen in (b) near 300 km.

plasma bubbles over China during the same storm on 7–8 September 2017 by using data from Global Navigation Satellite System networks. The TEC depletion was observed after 12:45 UT, consistent with the FAIs observed by the HCOPAR.

During the recovery phase of the geomagnetic storm, the postsunset equatorial plasma bubble is usually suppressed by overshielding westward electric field (Abdu et al., 2009), which can cause downward plasma drift and reduce the growth rate of R-T instability. Besides overshielding electric field, disturbance wind dynamoelectric field can also suppress the irregularities in the recovery phase. However, the observations described in the previous section indicate that irregularities can still be triggered even in the recovery phase of the storm, if an additional storm intensification accompanied IMF southward turning and penetration of eastward IEF to low-latitude occur in the dusk sector.

4.2. Postmidnight FAIs

Under quiet condition, the ambient zonal electric field is usually westward in the postmidnight period and can cause downward plasma drift, so it does not support the FAIs generation after local midnight. In this case, the irregularities persisted into the postmidnight sector when the southward IMF Bz gradually recovered to its quiet time values. As displayed in Figures 5e–5g, the FAIs emerged above 400 km (highlighted with red circles) were freshly generated in Beam 5 of HCOPAR after 16:15 UT and then drifted westward to Beams 6 and 7 with increasing echo intensity. These FAIs were Type 1 echoes and were still in growth phase. Figure 3a shows that the base height of *F* layer again started to lift at ~17:00 UT and reached a peak height of ~390 km at ~17:40 UT. During this period of bottomside *F* layer elevation, the strip-like FAIs (Group G in Figure 4a) were first recorded by Beam 1 of the radar, continuing to drift westward and being recorded by the other beams successively. These echoes were Type 2 echoes, which were generated outside of the radar beams and they remained in the FoV of HCOPAR for about 1 hr from ~17:00 to ~18:00 UT. Both the uplift of *F* layer and irregularities occurring after midnight serve as direct evidences for high-latitude electric field

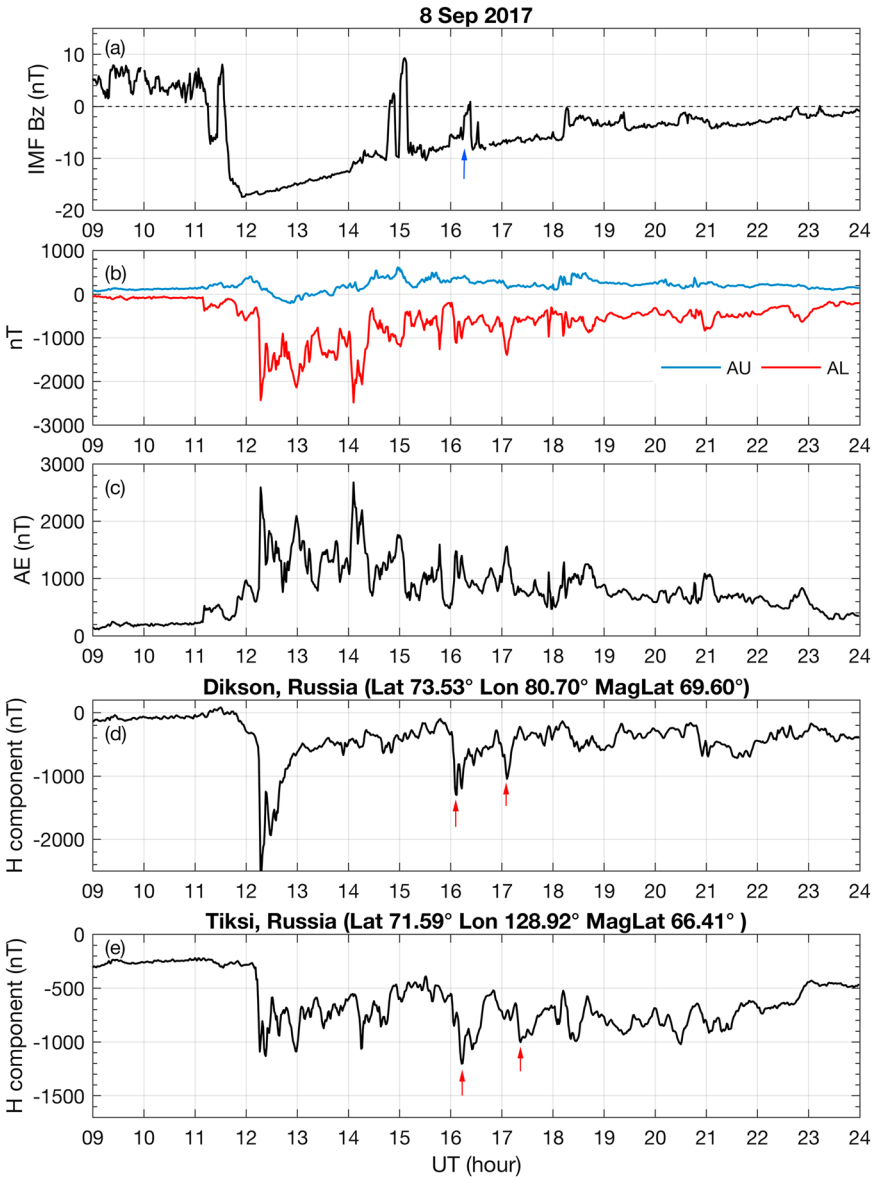

Figure 7. (a) Zoomed in version of the interplanetary magnetic field (IMF) Bz (nT), (b) AU (blue) and AL (red) indices (nT), (c) AE index (nT), (d) *H* component (nT) at Dikson, Russia (73.53°N, 80.70°E, magnetic latitude 69.06°N), (e) *H* component (nT) at Tiksi, Russia (71.59°N, 128.92°E, magnetic latitude 66.41°N). Blue arrow in (a) indicates the short period of IMF northward turning. Red arrows in (d) and (e) indicate the two consecutive substorm onsets.

penetrating to low-latitude ionosphere. As we discussed in the introduction section, undershielding PPEF has eastward (westward) polarity on the dayside (nightside) and overshielding PPEF has westward (eastward) polarity on the dayside (nightside). Therefore, eastward overshielding PPEF should be responsible for the uplift of *F* layer and subsequent irregularities in the postmidnight sector in this case.

Previous studies have demonstrated that overshielding electric field can be triggered not only by IMF Bz northward turning (Fujita et al., 2010) but also by a substorm onset (e.g., Hashimoto et al., 2011; Kikuchi et al., 2003; Wei et al., 2009). To investigate the possible cause of the overshielding PPEF after midnight, we present the zoomed-in IMF Bz, the auroral activity indices, that is, the AU/AL and AE indices, and the *H* component measured by two high-latitude magnetometers at Dikson, Russia (73.53°N, 80.70°E, magnetic latitude 69.04°N) and Tiksi, Russia (71.59°N,128.92°E; magnetic latitude 66.41°N), during 09:00–24:00 UT on 8 September in Figures 7a–7e, respectively. We looked at the magnetometers that are used to construct the

Time History of Events and Macroscale Interactions during Substorms real-time AE and selected the *H* component data from Dikson and Tiksi stations. The *H* component measured at these two stations showed the sharpest decrease, suggesting that they were closest to the substorm onset location and thus can better determine the accurate timing of substorm onset. As shown in Figure 7a, the IMF Bz exhibited northward excursion (marked by a blue arrow) during a short time period, which may cause eastward overshielding electric field on the nightside. However, the effect of the IMF Bz northward turning is expected to show up very quickly (a few minutes after the northward turning) instead of delaying for ~30–40 min. Therefore, it is likely that the small bump of base height of *F* layer (labeled with black arrow d) in Figure 3a was the result of overshielding electric field due to the IMF Bz sudden but short northward turning. Another factor should be responsible for the uplift of *F* layer after 17:00 UT. As displayed in Figures 7b and 7c, the AL and AE indices indicated that there were several substorm expansions with the AE index exceeding 1,000 nT after 16 UT. It is obvious in Figures 7d and 7e that there were two sharp decreases of *H* component (marked by red arrows) between 16:00 and 18:00 UT, suggesting two consecutive substorm onsets while the IMF Bz was gradually decreasing/recovering toward quiet time values. Therefore, the large uplift of *F* layer after 17:00 UT is likely resulted from overshielding PPEF, which was induced by substorm onset at ~17 UT. Wei et al. (2009) and Hashimoto et al. (2011) demonstrated that the overshielding electric field can be quickly established after a substorm onset even without the IMF Bz northward turning. Simulation results based on the Rice Convection Model also demonstrated that the overshielding electric field can be set up right after substorm onset (Zhang et al., 2009). Comparing with the postsunset echoes, the intensity of the postmidnight echoes was much weaker. This may be attributed to the much lower vertical density gradient in the postmidnight sector (Huba & Joyce, 2010), so the growth rate of the R-T instability is much lower in postmidnight period than that during the postsunset hours. Consequently, the postmidnight FAIs could not grow into strong upwelling plume structure like the postsunset ones.

In addition, a distinct feature of the storm time irregularities observed on 8 September at Fuke is that their zonal drift was westward except for the beginning period of the observation, which differs from the quiet time eastward velocities. Numerous studies (e.g., Yokoyama et al., 2004; Patra et al., 2014) have shown that the zonal drift of the nighttime plasma irregularities is eastward under quiet conditions. During magnetically disturbed conditions, the zonal velocities of plasma irregularities may slow down and/or even reverse to westward (Abdu et al., 2003; Basu et al., 2010; Ma & Maruyama, 2006; Patra et al., 2016). In general, the zonal motion of the irregularities follows that of the ambient plasma. As seen in Figure 3c, the zonal drift of the background plasma fluctuated between westward and eastward in the initial hours and it reversed from eastward to stable westward at ~12:45 UT. The irregularities observed by the HCOPAR initiated at ~12:45 UT and represented little or even no zonal drift at the beginning of the observation as shown in Figures 5d–5g. Subsequently, the irregularities traveled westward, moving together with the ambient plasma. Therefore, the irregularities zonal motion pattern described above can be attributed to the reversal of the background plasma zonal drift. Ma and Maruyama (2006) reported that a storm-induced super plasma bubble exhibited a much slower eastward drift velocity in contrast to the quiet time, and they attributed the slow eastward drift to the storm time westward zonal wind. Reversal of zonal drift of the storm time irregularities form large eastward to westward due to the disturbance dynamo effect was also studied by Patra et al. (2016). The westward turning of zonal drift velocities of the FAIs in our observation probably resulted from the storm-related thermospheric disturbance winds that have a strong westward component in low-latitude regions. Further studies are required to be conducted in terms of the storm time thermospheric disturbance winds effects in future work.

5. Conclusion

In this study, the low-latitude ionospheric irregularities formation and evolution in response to the 7–8 September 2017 geomagnetic storm have been analyzed using data from HCOPAR and Hainan digisonde. The second sudden southward turning of IMF Bz that caused intensification of the storm (in the recovery phase) resulted in prompt penetration of eastward IEF to low-latitude that enhanced the ambient zonal eastward electric field during postsunset sector resulting in the uplift of the *F* layer to higher altitudes, creating favorable conditions for the growth of R-T instability and the generation of the FAIs in the postsunset hours. Moreover, the elevation of base height of *F* layer recorded by the Hainan digisonde in the postmidnight sector and the postmidnight irregularities observed by HCOPAR are likely due to the substorm-related

overshielding electric field, which has eastward polarity on the night side. The zonal drift of the FAIs that usually follows the ambient plasma drift (normally eastward at night) was found to be near zero in the beginning and soon turned westward. The reversal of the background plasma zonal drift observed by Hainan digisonde is likely responsible to the unusual zonal drift pattern of storm time irregularities.

Acknowledgments
This project was supported by the National Natural Science Foundation of China (41722404 and 41474132). S. Zou acknowledges the support of NSF AGS1400998 and AGS1342968. The authors acknowledge the use of the Hainan coherent scatter radar and Hainan digisonde data from the Chinese Meridian Project (http://data.meridian-project.ac.cn/).The solar wind and IMF data as well as the SYM/H index are obtained from the OMNIWeb Data Explorer (https://omniweb.gsfc.nasa.gov/). The auroral activity indices AU/AL/AE are obtained from the World Data Center for Geomagnetism at Kyoto University (http://wdc.kugi.kyoto-u.ac.jp/). We thank Arctic and Antarctic Research Institute (AARI), Department of Geophysics (http://geophys.aari.ru) for use of the AARI magnetometers data.

References

Aa, E., Huang, W., Liu, S., Ridley, A. J., Zou, S., Shi, L., et al. (2018). Mid-latitude plasma bubble over China and adjacent areas during a magnetic storm on 08 September 2017. *Space Weather*, *16*. https://doi.org/10.1002/2017SW001766

Abdu, M. A. (2012). Equatorial spread *F*/plasma bubble irregularities under storm time disturbance electric fields. *Journal of Atmospheric and Solar: Terrestrial Physics*, *75*, 44–56.

Abdu, M. A., Batista, I. S., Takahashi, H., MacDougall, J., Sobral, J. H., Medeiros, A. F., & Trivedi, N. B. (2003). Magnetospheric disturbance induced equatorial plasma bubble development and dynamics: A case study in Brazilian sector. *Journal of Geophysical Research*, *108*(A12), 1449. https://doi.org/10.1029/2002JA009721

Abdu, M. A., Kherani, E. A., Batista, I. S., & Sobral, J. H. A. (2009). Equatorial evening prereversal vertical drift and spread *F* suppression by disturbance penetration electric fields. *Geophysical Research Letters*, *36*, L19103. https://doi.org/10.1029/2009GL039919

Abdu, M. A., Sastri, M. A., MacDougall, J., Batista, I. S., & Sobral, J. H. A. (1997). Equatorial disturbance dynamo electric field, longitudinal structure and spread *F*: A case study from GUARA/EITS campaigns. *Geophysical Research Letters*, *24*(13), 1707–1710.

Basu, S., Basu, S., Groves, K. M., Yeh, H. C., Su, S. Y., Rich, F. J., et al. (2001). Response of the equatorial ionosphere in the South Atlantic region to the great magnetic storm of July 15, 2000. *Geophysical Research Letters*, *28*(18), 3577–3580. https://doi.org/10.1029/2001GL013259

Basu, S., Basu, S., MacKenzie, E., Bridgwood, C., Valladares, C. E., Groves, K. M., & Carrano, C. (2010). Specification of the occurrence of equatorial ionospheric scintillations during the main phase of large magnetic storms within solar cycle 23. *Radio Science*, *45*, RS5009. https://doi.org/10.1029/2009RS004343

Blanc, M., & Richmond, A. D. (1980). The ionospheric disturbance dynamo. *Journal of Geophysical Research*, *85*(A4), 1669–1688. https://doi.org/10.1029/JA085iA04p01669

Burke, W. J., Gentile, L. C., Huang, C. Y., Valladares, C. E., & Su, S. Y. (2004). Longitudinal variability of equatorial plasma bubbles observed by DMSP and ROCSAT-1. *Journal of Geophysical Research*, *109*, A12301. https://doi.org/10.1029/2004JA010583

Chen, G., Jin, H., Yan, J., Cui, X., Zhang, S., Yan, C., et al. (2017). Hainan Coherent Scatter Phased Array Radar (HCOPAR): System design and ionospheric irregularity observations. *IEEE Transactions on Geoscience and Remote Sensing*, *55*(8), 4757–4765.

Chen, W. S., Lee, C. C., Liu, J. Y., Chu, F. D., & Reinisch, B. W. (2006). Digisonde spread *F* and GPS phase fluctuations in the equatorial ionosphere during solar maximum. *Journal of Geophysical Research*, *111*, A12305. https://doi.org/10.1029/2006JA011688

Fujita, S., Kikuchi, T., & Tanaka, T. (2010). State transition of the magnetosphere-ionosphere compound system due to a northward turn of the interplanetary magnetic field revealed from a global magnetohydrodynamic simulation and formation of the overshielding potential. *Journal of Geophysical Research*, *115*, A11210. https://doi.org/10.1029/2010JA015550

Hashimoto, K. K., Kikuchi, T., Watari, S., & Abdu, M. A. (2011). Polar-equatorial ionospheric currents driven by the region 2 field-aligned currents at the onset of substorms. *Journal of Geophysical Research*, *116*, A0921. https://doi.org/10.1029/2011JA016442

Heelis, R. A. (2004). Electrodynamics in the low and middle latitude ionosphere: A tutorial. *Journal of Atmospheric and Solar: Terrestrial Physics*, *66*(10), 825–838.

Hickey, D. A., Martinis, C. R., Rodrigues, F. S., Varney, R. H., Milla, M. A., Nicolls, M. J., et al. (2015). Concurrent observations at the magnetic equator of small-scale irregularities and large-scale depletions associated with equatorial spread *F*. *Journal of Geophysical Research: Space Physics*, *120*, 10,883–10,896. https://doi.org/10.1002/2015JA021991

Huang, C.-S., de La Beaujardiere, O., Roddy, P. A., Hunton, D. E., Ballenthin, J. O., & Hairston, M. R. (2012). Generation and characteristics of equatorial plasma bubbles detected by the C/NOFS satellite near the sunset terminator. *Journal of Geophysical Research*, *117*, A11313. https://doi.org/10.1029/2012JA018163

Huang, C.-S., de La Beaujardiere, O., Roddy, P. A., Hunton, D. E., Liu, J. Y., & Chen, S. P. (2014). Occurrence probability and amplitude of equatorial ionospheric irregularities associated with plasma bubbles during low and moderate solar activities (2008–2012). *Journal of Geophysical Research: Space Physics*, *119*, 1186–1199. https://doi.org/10.1002/2013JA019212

Huba, J. D., & Joyce, G. (2010). Global modeling of equatorial plasma bubbles. *Geophysical Research Letters*, *37*, L17104. https://doi.org/10.1029/2010GL044281

Kikuchi, T., Hashimoto, K. K., Kitamura, T.-I., Tachihara, H., & Fejer, B. (2003). Equatorial counterelectrojets during substorms. *Journal of Geophysical Research*, *108*(A11), 1406. https://doi.org/10.1029/2003JA009915

Kikuchi, T., Hashimoto, K. K., & Nozaki, K. (2008). Penetration of magnetospheric electric fields to the equator during a geomagnetic storm. *Journal of Geophysical Research*, *113*, A06214. https://doi.org/10.1029/2007JA012628

Kil, H., & Heelis, R. A. (1998). Global distribution of density irregularities in the equatorial ionosphere. *Journal of Geophysical Research*, *103*(A1), 407–417. https://doi.org/10.1029/97JA02698

Lee, C. C., Liu, J. Y., Reinisch, B. W., Chen, W. S., & Chu, F. D. (2005). The effects of the pre-reversal E × B drift, the EIA asymmetry, and magnetic activity on the equatorial spread *F* during solar maximum. *Annales de Geophysique*, *23*(3), 745–751.

Li, G., Ning, B., Abdu, M. A., Otsuka, Y., Yokoyama, T., Yamamoto, M., & Liu, L. (2013). Longitudinal characteristics of spread *F* backscatter plumes observed with the EAR and Sanya VHF radar in Southeast Asia. *Journal of Geophysical Research: Space Physics*, *118*, 6544–6557. https://doi.org/10.1002/jgra.50581

Li, G., Ning, B., Hu, L., Liu, L., Yue, X., Wan, W., et al. (2010). Longitudinal development of low-latitude ionospheric irregularities during the geomagnetic storms of July 2004. *Journal of Geophysical Research*, *115*, A04304. https://doi.org/10.1029/2009JA014830

Ma, G., & Maruyama, T. (2006). A super bubble detected by dense GPS network at east Asian longitudes. *Geophysical Research Letters*, *33*, L21103. https://doi.org/10.1029/2006GL027512

Martinis, C. R., Mendillo, M. J., & Aarons, J. (2005). Toward a synthesis of equatorial spread *F* onset and suppression during geomagnetic storms. *Journal of Geophysical Research*, *110*, A07306. https://doi.org/10.1029/2003JA010362

Nishida, A. (1968). Coherence of geomagnetic DP 2 fluctuations with interplanetary magnetic variations. *Journal of Geophysical Research*, *73*(17), 5549–5559. https://doi.org/10.1029/JA073i017p05549

Otsuka, Y., Shiokawa, K., Ogawa, T., Yokoyama, T., Yamamoto, M., & Fukao, S. (2004). Spatial relationship of equatorial plasma bubbles and field-aligned irregularities observed with an all-sky airglow imager and the Equatorial Atmosphere Radar. *Geophysical Research Letters*, *31*, L20802. https://doi.org/10.1029/2004GL020869

Ott, E. (1978). Theory of Rayleigh-Taylor bubbles in the equatorial ionosphere. *Journal of Geophysical Research*, *83*(A5), 2066.
Patra, A. K., Chaitanya, P. P., Dashora, N., Sivakandan, M., & Taori, A. (2016). Highly localized unique electrodynamics and plasma irregularities linked with the 17 March 2015 severe magnetic storm observed using multitechnique common-volume observations from Gadanki, India. *Journal of Geophysical Research: Space Physics*, *121*, 11,518–11,511. https://doi.org/10.1002/2016JA023384
Patra, A. K., Srinivasulu, P., Chaitanya, P. P., Rao, M. D., & Jayaraman, A. (2014). First results on low-latitude *E* and *F* region irregularities obtained using the Gadanki Ionospheric Radar Interferometer. *Journal of Geophysical Research: Space Physics*, *119*, 10,276–10,210. https://doi.org/10.1002/2014JA020604
Pi, X., Mannucci, A. J., Lindqwister, U. J., & Ho, C. M. (1997). Monitoring of global ionospheric irregularities using the worldwide GPS network. *Geophysical Research Letters*, *24*(18), 2283–2286.
Rajesh, P. K., Lin, C. H., Chen, C. H., Lin, J. T., Matsuo, T., Chou, M. Y., et al. (2017). Equatorial plasma bubble generation/inhibition during 2015 St. Patrick's Day storm. *Space Weather*, *15*, 1141–1150. https://doi.org/10.1002/2017SW001641
Rastogi, R. G. (1980). Seasonal variation of equatorial spread *F* in the American and Indian zones. *Journal of Geophysical Research: Space Physics*, *85*(A2), 722–726.
Reinisch, B. W., Galkin, I. A., Khmyrov, G. M., Kozlov, A. V., Bibl, K., Lisysyan, I. A., et al. (2009). New Digisonde for research and monitoring applications. *Radio Science*, *44*, RS0A24. https://doi.org/10.1029/2008RS004115
Reinisch, B. W., Scali, J. L., & Haines, D. L. (1998). Ionospheric drift measurements with ionosondes. *Annali di Geofisica*, *41*, 695–702.
Shen, C., Chi, Y., Wang, Y., Xu, M., & Wang, S. (2017). Statistical comparison of the ICME's geoeffectiveness of different types and different solar phases from 1995 to 2014. *Journal of Geophysical Research: Space Physics*, *122*, 5931–5948. https://doi.org/10.1002/2016JA023768
Shen, C., Xu, M., Wang, Y., Chi, Y., & Luo, B. (2018). Why the Shock-ICME Complex Structure is Important: Learning From the Early 2017 September CMEs. arXiv preprint arXiv:1805.05763.
Sobral, J. H. A., Abdu, M. A., Pedersen, T. R., Castilho, V. M., Arruda, D. C. S., Muella, M. T. A. H., et al. (2009). Ionospheric zonal velocities at conjugate points over Brazil during the COPEX campaign: Experimental observations and theoretical validations. *Journal of Geophysical Research*, *114*, A04309. https://doi.org/10.1029/2008JA013896
Tsunoda, R. T. (1980). On the spatial relationship of 1-m equatorial spread *F* irregularities and plasma bubbles. *Journal of Geophysical Research*, *85*(A1), 185–190.
Tulasi Ram, S., Rama Rao, P. V. S., Prasad, D. S. V. V. D., Niranjan, K., Gopi Krishna, S., Sridharan, R., & Ravindran, S. (2008). Local time dependent response of postsunset ESF during geomagnetic storms. *Journal of Geophysical Research*, *113*, A07310. https://doi.org/10.1029/2007JA012922
Wang, C. (2010). New chains of space weather monitoring stations in China. *Space Weather*, *8*, S08001. https://doi.org/10.1029/2010SW000603
Wei, Y., Pu, Z., Hong, M., Zong, Q., Ren, Z., Fu, S., et al. (2009). Westward ionospheric electric field perturbations on the dayside associated with substorm processes. *Journal of Geophysical Research*, *114*, A12209. https://doi.org/10.1029/2009JA014445
Woodman, R. F. (1970). Vertical drift velocities and east-west electric fields at the magnetic equator. *Journal of Geophysical Research*, *75*(31), 6249–6259. https://doi.org/10.1029/JA075i031p06249
Woodman, R. F. (2009). Spread *F*—An old equatorial aeronomy problem finally resolved? *Annales de Geophysique*, *27*(5), 1915–1934.
Woodman, R. F., & LaHoz, C. (1976). Radar observations of *F* region equatorial irregularities. *Journal of Geophysical Research*, *81*(31), 5447–5461.
Yokoyama, T., Fukao, S., & Yamamoto, M. (2004). Relationship of the onset of equatorial *F* region irregularities with the sunset terminator observed with the Equatorial Atmosphere Radar. *Geophysical Research Letters*, *31*, L24804. https://doi.org/10.1029/2004GL021529
Yokoyama, T., & Fukao, S. (2006). Upwelling backscatter plumes in growth phase of equatorial spread *F* observed with the Equatorial Atmosphere Radar. *Geophysical Research Letters*, *33*, L08104. https://doi.org/10.1029/2006GL025680
Zhang, J.-C., Wolf, R. A., Spiro, R. W., Erickson, G. M., Sazykin, S., Toffoletto, F. R., & Yang, J. (2009). Rice Convection Model simulation of the substorm-associated injection of an observed plasma bubble into the inner magnetosphere: 2. Simulation results., *Journal of Geophysical Research*, *114*, A08219. https://doi.org/10.1029/2009JA014131